

# Acrylic Attenuation Measurements for the MiniCLEAN Dark Matter Detector

Author:  
Nguyen Phan

Advisors:  
Keith Rielage (LANL)  
Dinesh Loomba  
John Matthews

Undergraduate Honors Thesis  
University of New Mexico  
Department of Physics and Astronomy  
April 24, 2009

## Abstract

The MiniCLEAN dark matter detection experiment aims to detect the signature of a WIMP-nucleus interaction by utilizing a 400 kg spherical target volume of liquid argon surrounded by 92 photomultiplier tubes (PMTs). The glass of the PMTs that are used to detect the interaction signal poses a challenge as it contains low levels of radioactivity sufficient to produce a significant neutron background. Although progress is being made in producing glass with lower levels of radioactivity, PMTs will still be the dominant neutron source given their close proximity to the target volume. Acrylic light guides are placed between the PMTs and the liquid argon to attenuate neutrons from the PMTs and prevent them from leaking into the target volume and producing false signal detections.

Because the UV scintillation light ( $\sim 128$  nm) produced by the WIMP interaction in the target volume cannot penetrate the acrylic rods, the acrylic surface in contact with the liquid argon is coated with tetraphenyl butadiene (TPB), a wavelength shifter that converts the liquid argon scintillation light into the visible spectrum, which can travel through the acrylic rod to the PMT. Proper signal discrimination and event reconstruction requires the characterization of the optical properties of these acrylic light guides because the interaction signals must travel through the acrylic for detection. The distribution of light among the PMTs is used to determine the origin of the event which provides a means to discriminate between WIMP and neutron interactions.

In this experiment, eight cylindrical acrylic rods approximately one meter long from three different manufacturers were obtained and the attenuation lengths of each rod were determined at five wavelengths of light (375 nm, 405 nm, 440 nm, 543 nm, and 632 nm). This was accomplished by placing each rod between a laser and photometer and measuring the power reduction of the laser light after passing through the acrylic. The measurements found inconsistencies in the attenuation lengths between samples from different manufacturers as well as samples from the same manufacturer. MiniCLEAN is recommended to test each of its light guides individually because the attenuation determined for one sample cannot be reliably applied to the other samples even if they originate from the same manufacturer.

# Table of Contents

<b>1</b>	<b>Introduction</b>	<b>6</b>
<b>2</b>	<b>Astronomical and Theoretical Motivations</b>	<b>6</b>
2.1	Observational Evidence . . . . .	6
2.1.1	Velocity Dispersion in Galaxy Clusters . . . . .	7
2.1.2	Gravitational Lensing in the Bullet Cluster . . . . .	8
2.1.3	WMAP Observations . . . . .	10
2.2	Quest for Direct Detection . . . . .	11
2.2.1	Earth-Based Detection . . . . .	11
2.2.2	Astronomical Constraints . . . . .	11
2.2.3	Theoretical Constraints . . . . .	12
<b>3</b>	<b>Noble Liquid Detectors</b>	<b>13</b>
3.1	Signal Detection and Discrimination . . . . .	13
3.2	Signal Discrimination . . . . .	14
3.3	Single Phase vs. Two-Phase Detectors . . . . .	14
<b>4</b>	<b>MiniCLEAN</b>	<b>16</b>
4.1	Goals of the CLEAN Detection Program . . . . .	17
4.2	Design of MiniCLEAN . . . . .	18
4.3	Backgrounds . . . . .	20
4.3.1	Cosmic-Ray Induced Neutrons . . . . .	21
4.3.2	Local Sources of Backgrounds . . . . .	22
<b>5</b>	<b>Acrylic Attenuation</b>	<b>22</b>
5.1	Definitions . . . . .	23
5.2	Previous Acrylic Measurements . . . . .	24
5.2.1	SNO . . . . .	24
5.2.2	Daya Bay . . . . .	25
5.3	Acrylic Samples . . . . .	26
5.4	Experimental Setup . . . . .	26
5.5	Experimental Procedure . . . . .	28
5.6	Systematic Uncertainties . . . . .	30
5.7	Results . . . . .	31
5.8	Discussion . . . . .	33
5.9	Conclusions . . . . .	42
<b>6</b>	<b>Acknowledgments</b>	<b>43</b>
	<b>References</b>	<b>44</b>

## List of figures

1	Bullet Cluster . . . . .	9
2	Nuclear Recoil Diagram . . . . .	12
3	Excimer Formation . . . . .	14
4	Ratio of Early to Late Light . . . . .	15
5	Schematic of the XENON10 Detector . . . . .	16
6	Plot of WIMP cross-section limits . . . . .	17
7	Inner Vessel of the MiniCLEAN Detector . . . . .	19
8	Optical Cassette Design . . . . .	19
9	MiniCLEAN Detector Assembly . . . . .	20
10	Plot of Depths of Underground Laboratories . . . . .	21
11	TPB spectrum . . . . .	23
12	SNO acrylic transmittance curves . . . . .	25
13	Diagram of Experimental Setup . . . . .	27
14	Transmittance Plot for Spartech Samples Without Lens . . . . .	35
15	Transmittance Plot for Spartech Samples With Lens . . . . .	36
16	Transmittances of Rohm Samples Without Lens . . . . .	37
17	Transmittances of Rohm Samples With Lens . . . . .	38
18	RPT Transmittance Without Lens . . . . .	39
19	RPT Transmittance With Lens . . . . .	40
20	Best Performing Rod From Each Manufacturer Without Lens . . . . .	41
21	Best Performing Sample From Each Manufacturer With Lens . . . . .	41

## List of Tables

1	Singlet and Triplet Lifetimes . . . . .	13
2	Total Reflectance . . . . .	28
3	A Sample Measurement Set . . . . .	29
4	Spartech Attenuation Lengths Without Lens . . . . .	32
5	Spartech Attenuation Lengths With Lens . . . . .	32
6	Rohm Attenuation Lengths Without Lens . . . . .	32
7	Rohm Attenuation Lengths With Lens . . . . .	33
8	RPT Attenuation Lengths Without Lens . . . . .	33
9	RPT Attenuation Lengths With Lens . . . . .	33
10	Transmittances of Spartech Samples Without Lens . . . . .	34
11	Transmittance of Spartech Samples With Lens . . . . .	35
12	Transmittances of Rohm Samples Without Lens . . . . .	37
13	Transmittance of Rohm Samples With Lens . . . . .	38
14	Transmittances of RPT Samples Without Lens . . . . .	39

15	Transmittances of RPT Samples With Lens . . . . .	40
----	---	----

# 1 Introduction

Dark matter has been a problem for over 75 years since Zwicky observed the motions of member galaxies of the Coma Cluster. Since Zwicky's observations, further astronomical observations of systems ranging in size from galaxies to the largest superclusters indicate the need for a paradigm shift: either there exist new, mysterious forms of non-luminous, 'dark matter', or there need to be modifications of our theory of gravity. In Chapter 2, I will review the observational evidence and theoretical motivations for dark matter. The leading hypothesis for dark matter that has been theorized over the past few decades is that dark matter is a new weakly-interacting, elementary particle. In Chapter 3, I will describe the MiniCLEAN (Cryogenic Low Energy Astrophysics with Noble Liquids) dark matter detector, which is designed to look for such particles. The main problem encountered by all dark matter detection experiments involves separation of radioactive backgrounds from signals and any viable technology must have robust methods to discriminate between these. In Chapter 4, I review the background rejection technology and methods employed in MiniCLEAN and outline the importance of acrylic light guides to shield against neutrons from the inherent radioactivity in the photo-multiplier tubes used to measure dark matter signals. The acrylic light guides are central to this thesis. These light guides not only must shield against the neutrons at a sufficiently high level, but also serve the purpose of transmitting light to the phototubes with maximal efficiency. Significant loss of light in the light-guides would compromise the entire experimental effort as the feeble dark matter signals would fall below the level of detectability needed to make MiniCLEAN a competitive experiment. Therefore, characterizing the optical properties of acrylic being considered for procurement for the light guides and designing a method to do this in a quick but robust manner is essential for the experiment. In Chapter 5, I describe my work on measuring the attenuation lengths of sample acrylic rods at multiple wavelengths, which also resulted in a recipe for the collaboration and others to use for this purpose. Finally, I summarize the conclusions drawn from these measurements.

## 2 Astronomical and Theoretical Motivations

### 2.1 Observational Evidence

It is currently believed that the matter content of the universe is dominated by an unknown material generally referred to as dark matter. The first indication of the existence of this pervasive yet non-luminous matter dates back over 75 years (Carroll & Ostlie). In 1933, while observing the motion of galaxies in the Coma cluster, a rich cluster of galaxies about 90 Mpc ( $\sim 294$  million light years)

away from Earth and containing perhaps 10,000 members within a diameter of 6 Mpc, Fritz Zwicky noticed that the velocity dispersion of the constituent galaxies was very high (Carroll & Ostlie). He hypothesized that there must be an extra component of the cluster's total mass which far exceeds the total luminous mass if the cluster was gravitationally bound. In the cosmological timescale, the fact that the cluster is still observed in the present era implies that this is likely the case because if the galaxies are not bound by mutual gravitation, then the cluster should have dispersed long ago. However, for many years, this discovery was largely ignored. It was not until decades later that new and corroborative evidence from measurements of the rotation curves of spiral galaxies, detections of gravitational lensing, and observations of the Cosmic Microwave Background made by the Wilkinson Microwave Anisotropy Probe (WMAP) strongly indicated that a considerable amount of the mass in galaxies and galaxy clusters could not be accounted for by luminous matter alone. These combined observations are motivating the present challenging endeavor for direct dark matter detection.

### 2.1.1 Velocity Dispersion in Galaxy Clusters

The non-luminous nature of dark matter poses a considerable challenge to astronomical observation. In fact, its existence can only be detected indirectly through its gravitational effects on the kinematics of ordinary, luminous matter. The method used by Zwicky to estimate the mass of the Coma cluster is an application of this concept. The principle assumption underlying its usage is that the cluster of interest is in virial equilibrium, and therefore, obeys the virial theorem which is given by

$$2\langle K \rangle + \langle U \rangle = 0,$$

where  $K$  is the kinetic energy and  $U$  is the potential energy of the system. This relation can be re-expressed as

$$-2 \sum_{i=1}^N \frac{1}{2} m_i v_i^2 = U,$$

where  $m_i$  and  $v_i$  represent the mass and velocity, respectively, of each of the cluster's galaxies, and  $N$  is the total number of members. If we also assume that each member galaxy has the same mass and we divide by the number of members, the above expression becomes

$$-\frac{m}{N} \sum_{i=1}^N v_i^2 = \frac{U}{N}.$$

Relating the square magnitude of the velocity to the velocity dispersion,  $\sigma_r$ ,

$$\frac{1}{N} \sum_{i=1}^N v_i^2 = \langle v^2 \rangle = 3 \langle v_r^2 \rangle = 3\sigma_r^2$$

and using the fact that the total gravitational potential energy in the cluster is approximately given by

$$U_g = -\frac{3}{5} \frac{GM^2}{R},$$

which results from assuming that the density of the cluster is constant and equals its average value ( $\rho = \frac{M}{(4/3)\pi R^3}$ ), we arrive at an estimate of the cluster mass through the expression

$$M_{vir} \approx \frac{5R\sigma_r^2}{G}$$

(Carroll & Ostlie). The velocity dispersion is calculated from measurements of the radial velocities of constituent galaxies from the Doppler shifts of their spectral lines. The radius can be derived either from measuring the distance to the cluster using Type Ia supernovae as standard candles, or the Hubble Law which relates the cluster's distance to its recessional velocity. Once the distance to the cluster is known, its linear size can be derived from the observed angular size. Recent observations suggest a value of  $977 \text{ km/s}$  for the Coma cluster's velocity dispersion, implying a cluster mass of  $3.3 \times 10^{15} M_\odot$  ( $1M_\odot = 1 \text{ solar mass} = 1.9891 \times 10^{30} \text{ kg}$ ) (Carroll & Ostlie). Strikingly, an estimate of the cluster's luminous mass which consists predominantly of intracluster gas, gives a value of only  $10^{14} M_\odot$ , an entire order of magnitude below the expected mass. This suggests that the principal mass component of the Coma cluster is of a non-luminous form.

### 2.1.2 Gravitational Lensing in the Bullet Cluster

The kinematics of astrophysical objects ranging in size from galaxies to clusters of galaxies indicates the presence of large component of missing mass. This conclusion derives from our theory of gravity, but what if this theory is invalid at certain distance scales? If this is the case, the dark matter phenomenon could merely be an artifact of our limited understanding of gravity. Such is the argument put forth by opponents of the so called dark matter paradigm. They have been persistent in their suggestion that the observations described earlier can be explained not by missing mass, but by a modification to the law of gravitation. This alternative explanation to the missing mass problem, first proposed by Milgrom and Bekenstein in the early 1980s, is known as Modified Newtonian Dynamics (MOND) (Dai et al.). Although the theory has achieved a measure of success by explaining flat galactic rotation curves and other kinematical observations related to dark matter, the discovery of the colliding galaxy cluster 1E0657-56, more commonly referred to as the Bullet Cluster, has cast doubts on its validity.

It is known from observation that  $\sim 90\%$  of the visible mass in galaxy clusters is in the form of ionized hydrogen gas that permeates its entire volume, and with

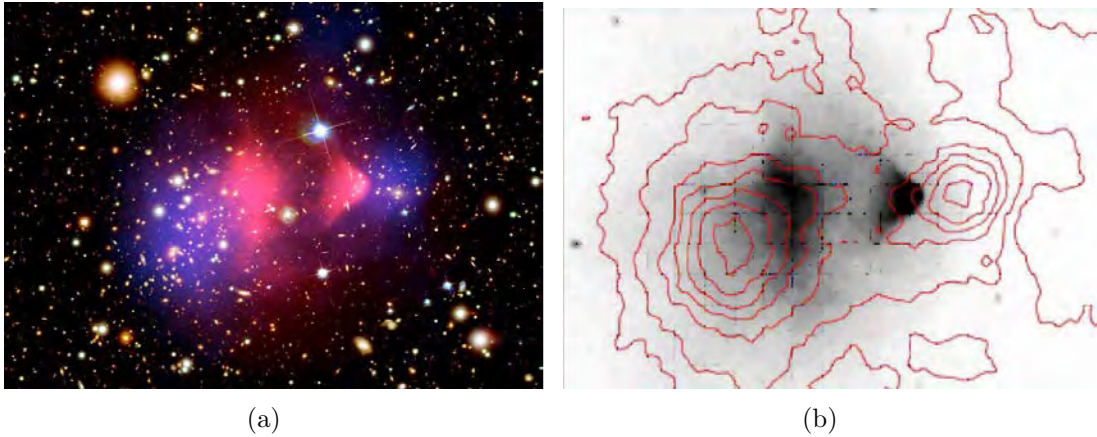


Figure 1: (a) The x-ray emission of ionized hydrogen (pink) in the Bullet cluster overlaid on an optical image. The blue regions represent mass concentrations as deduced from weak lensing observations. (b) The ionized hydrogen is characterized in this image by the darker regions while the contours trace out the mass concentrations (Clowe et al.).

the remaining mass in the form of stars (Clowe et al.). Because of the large distances between stars in galaxies and between galaxies in the cluster, galaxies can essentially be regarded as collisionless objects during collisions between clusters. Conversely, the ionized gas is extremely collisional because of its pervasiveness in the cluster. As a result, the hot gas will be slowed down by ram pressure while the collisionless galaxies will undergo little interaction during a cluster merger. This causes the gas to trail the leading galaxies as the interacting clusters move away from one another. The dark matter in the cluster is also believed to be collisionless because of its weakly interacting nature and consequently should be located near the galaxies after the interaction. By separating the plasma, which is the dominant source of gravitational mass in the luminous component, from the galaxies and the hypothesized dark matter, this system provides an ideal test of dark matter versus MOND. The dark matter hypothesis would predict that the major component of mass seen from gravitational lensing would reside close to the galaxies, whereas MOND would predict that it resides in the plasma. X-ray observations mapping the plasma distribution of the cluster and gravitational lensing observations resolving the lensing center of the Bullet cluster are in agreement with what would be expected if, indeed, the inferred missing mass in galaxies and galaxy clusters is due to dark matter and not modified gravity (Clowe et al.). In figure 1b, the plasma is represented by the darker regions while the overlying contours are the results of weak lensing observations, showing that the lensing centers

do not coincide with the bulk of the luminous mass. This observation cannot be explained solely by modified gravity and is widely regarded as the single best piece of evidence for the existence of dark matter.

### 2.1.3 WMAP Observations

The reigning cosmological model posits that the universe underwent a phase of rapid expansion after the Big Bang, a period known as inflation. According to the inflationary model, the universe must be spatially flat and has total density  $\Omega_0$ , in units of the critical density, equal to unity. The density parameter is defined as

$$\Omega_0 = \frac{\rho_0}{\rho_{0,c}},$$

where  $\rho_0$  is the present value required for a spatially flat universe and  $\rho_{0,c}$  is the present value of the critical density (Carroll & Ostlie). The results from the Wilkinson Microwave Anisotropy Probe (WMAP), which was designed to measure tiny temperature fluctuations in the Cosmic Microwave Background Radiation, does in fact support this assertion, giving a value of  $\Omega_0 = 1.02 \pm 0.02$  (Carroll & Ostlie). WMAP measurements of the temperature anisotropies also constrain the total matter density and the density in baryons, or ordinary matter composed of protons and neutrons. The results for these are  $\Omega_m = 0.27 \pm 0.04$  and  $\Omega_b = 0.044 \pm 0.004$ , where  $\Omega_m$  is the total density parameter for all matter content and  $\Omega_b$  is the density parameter for baryonic matter (Carroll & Ostlie). The observations also suggested that the density of all relativistic particles is  $8.24 \times 10^{-5}$  (Carroll & Ostlie). The density of something called dark energy makes up the remaining contribution to the total density. The nature of dark energy, which is hypothesized to explain the acceleration of the universe inferred from measurements of Type 1a supernovae, is unknown and outside the scope of this thesis. The scale of the temperature fluctuations observed by WMAP were, in fact, predicted by theories that incorporated dark matter as the dominant matter component. In these theories, structure formation in the universe requires dark matter composed of cold (i.e. non-relativistic), weakly-interacting particles. Neither baryons, nor neutrinos, which are relativistic and would be classified as a hot dark matter component, can explain the structure observed in the universe today (Carroll & Ostlie). Currently, the cold dark matter (CDM) model provides the best fit with observations and provides motivation for efforts to detect the non-baryonic particles responsible for dark matter.

## 2.2 Quest for Direct Detection

### 2.2.1 Earth-Based Detection

The preponderance of the present astronomical evidence suggests that the largest component of matter in the universe exists as non-radiating and weakly-interacting particles. But to unequivocally verify this hypothesis, a direct detection of the particle responsible for the missing mass phenomenon observed in galaxies and clusters is needed. The quest to accomplish this is among the many endeavors leading to the continually increasing partnership between two separate disciplines, astrophysics and elementary particle physics. It would appear that a direct detection in a laboratory on Earth would create little difficulty since astronomical evidence reveals that dark matter is the most ubiquitous and abundant form of matter in the universe. However, it is believed that the dark matter particle, somewhat similar to neutrinos, only interacts through the weak force, and should therefore have an extremely small cross-section for interacting with target materials in Earth-based laboratories. In this way, dark matter detection efforts are very challenging and quite similar to solar and cosmic neutrino detection experiments.

### 2.2.2 Astronomical Constraints

Astronomical observations and models of the mass distribution in our Galaxy, suggests that it, like all other galaxies, is surrounded by a halo of dark matter particles. This halo encompasses a region much larger than the luminous disk and persists to the present time because of the inability of dark matter particles to lose energy radiatively and collapse to form more compact objects (Cline). As the Earth moves through this cloud of dark particles, we expect a flux of these particles streaming through the Earth (Cline). Measurements of the Galactic rotation curve give an estimate of the local dark matter density to be about  $0.3 \text{ GeV}/\text{cm}^3$  (Rich). The Earth moves through the Galaxy at approximately  $230 \text{ km}/\text{s}$ , implying a local flux of  $10^7(1 \text{ GeV}/m_\chi) \text{ cm}^{-2}\text{s}^{-1}$ , where  $m_\chi$  is the mass of the dark matter particle (Rich). Direct detection experiments endeavor to detect these particles as they stream through the planet by monitoring their interactions with the target material of the detector. Yet constraints must be placed on their mass and cross-section in order to properly design detectors to look for such particles and to be able to distinguish their interactions from those caused by other particles. These constraints, provided by particle physics, help to narrow down the search for these elusive particles. Thus, the quest to understand the nature of dark matter has spread outside the domains of astronomical research and into the area of particle physics.

### 2.2.3 Theoretical Constraints

Some extensions of the well-established Standard Model of particle physics, most notably Supersymmetric (SUSY) theory, predict an ensemble of new supersymmetric particles, all of which have yet to be detected. But among these new particles, a small class appears to possess the essential characteristics that qualify them as dark matter candidates. These candidates are collectively known as WIMPs or Weakly Interacting Massive Particles. As their name suggests, these particles interact, beside gravitationally, only through the weak interaction and consequently do not radiate light. Current WIMP detection efforts are all concentrated on detecting the lightest of the supersymmetric particles called the neutralino, a neutral particle predicted to be stable by SUSY. These detection efforts employ slightly different techniques but almost all are aimed at detecting the result of a nuclear recoil event in the detector target material due to an interaction with a WIMP. Thus far, no definitive detection has been made because of the extremely small cross-section for WIMP-nucleon interaction and the difficulty and cost in scaling up these existing detectors to large target masses to achieve the high sensitivities needed to reach predicted cross-sections. However, the continual improvements in present detector technologies and the development of new ones present a very promising future for dark matter detection efforts.

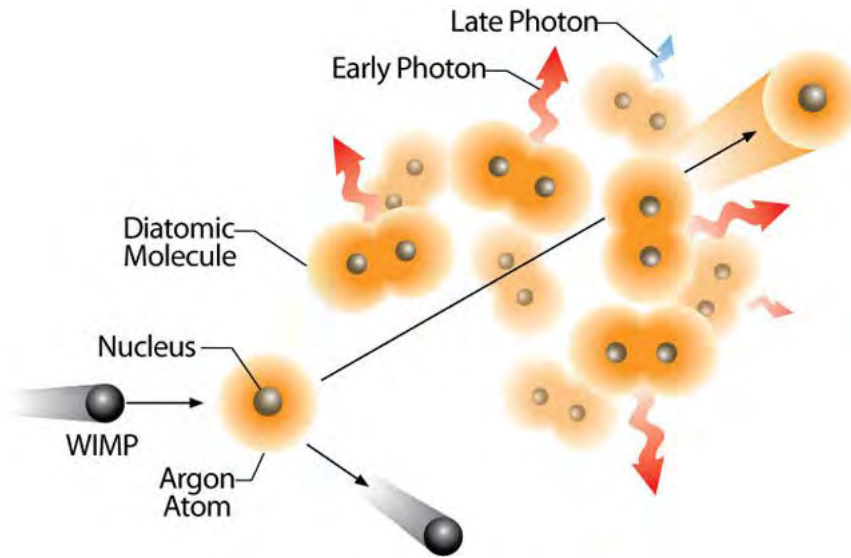
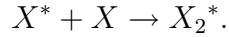


Figure 2: A diagram showing the interaction of a WIMP with a nucleus in the target material (argon). The recoiling nucleus creates excimers in the singlet and triplet states which eventually radiate early time and late time photons, respectively.

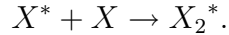
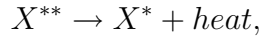
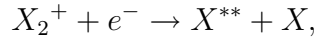
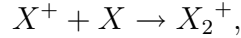
## 3 Noble Liquid Detectors

### 3.1 Signal Detection and Discrimination

Of particular promise are the noble liquid detectors such as MiniCLEAN (Cryogenic Low Energy Astrophysics with Noble Liquids) and DEAP (Dark Matter Experiment using Argon Pulse-shape discrimination), which aim to detect the signature of the elastic scattering of a WIMP from a nucleus by measuring the scintillation light caused by the recoiling nucleus. When a WIMP collides with a nucleus in the target material, the recoiling nucleus produces excitons and ions along its path. The excitons subsequently form excimers by combining with the ground state atoms through the following process (Mei et al.):



The ions also form excimers through a sequence of processes (Mei et al.):



These excimers form in either the singlet or triplet state and eventually decay down to the ground state, releasing scintillation light in the process. Table 1 lists the lifetimes for the singlet and triplet states of neon, argon, and xenon (Mei et al.).

		Lifetime (ns)	
	Singlet	Triplet	
Ne	$<18.2 \pm 0.2$	$14900 \pm 300$	
Ar	$7.0 \pm 1.0$	$1600 \pm 100$	
Xe	$4.3 \pm 0.6$	$22.0 \pm 2.0$	

Table 1: The lifetimes of the singlet and triplet excimers for liquid neon, argon, and xenon. The difference in the lifetimes of the two excimer states is the basis of the pulse-shape discrimination method.

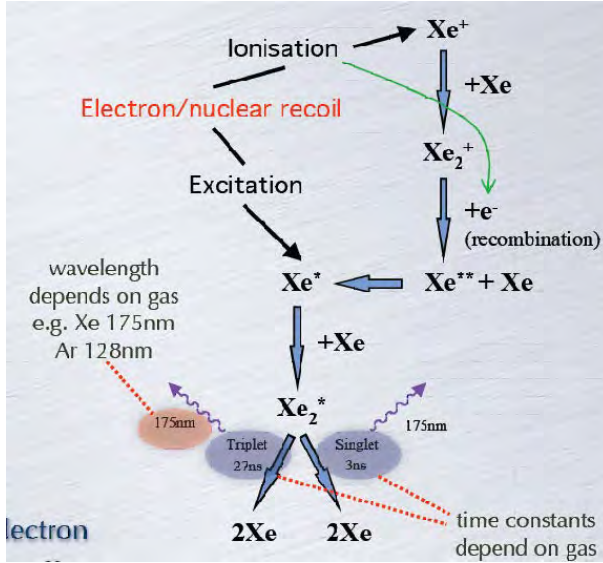


Figure 3: A diagram showing the various processes that lead to excimers after an interaction in a xenon target. The same processes occur in liquid argon and neon (Smith).

### 3.2 Signal Discrimination

The different lifetimes of these two states provide the possibility of discriminating scintillation light produced by a neutron or WIMP interaction from that produced by an electron or other light ionizers through a method called pulse-shape discrimination (PSD) (Lippincott et al.). The fraction of singlet to triplet excimers is different for WIMP/neutron nuclear recoils and electron recoils because triplet interactions are less probable for high excitation densities produced by interactions caused by a WIMP or neutron (Lippincott et al.). For example, in liquid argon, 70% of the excimers created by a WIMP/neutron induced nuclear-recoil are in the singlet state, whereas the ratio is  $\sim 30\%$  for electron induced recoils (Saab). So the ratio of early light to total light is characteristically higher for WIMP/neutron nuclear-recoils. Because the scattering process can vary from event to event, there is a statistical distribution of the fraction of singlet to triplet states. The plot in figure 4 is taken from the MiniCLEAN Conceptual Design Report (MC CDR) showing a distinctly different distribution of the ratio of early to total light for electron and WIMP/neutron recoils.

### 3.3 Single Phase vs. Two-Phase Detectors

A sub class of the noble liquid detectors, usually referred to as dual-phase, relies on a compound approach to event discrimination. These detectors (XENON10

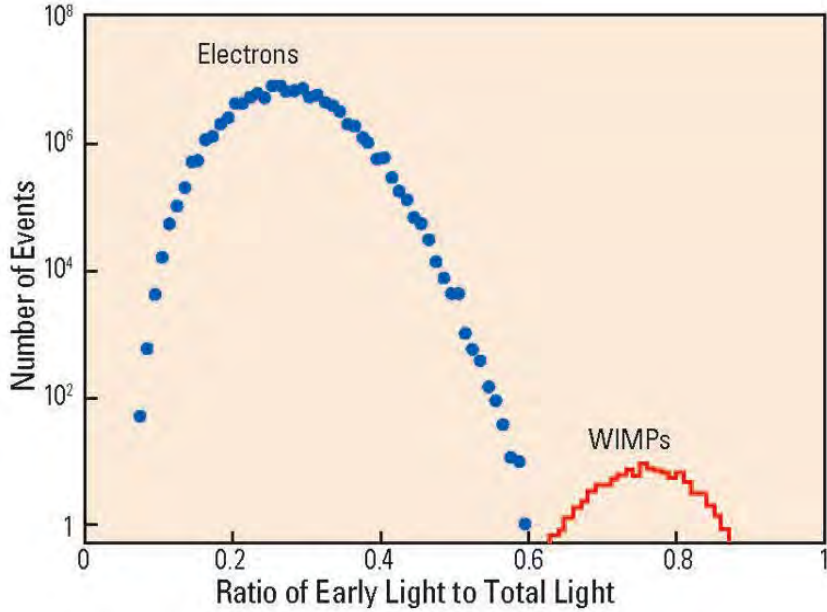


Figure 4: The distribution of the ratio of early to total light for WIMP/neutron and electron interactions based on simulations. The simulated data is for  $10^8$  events but discrimination should still be possible at  $10^{10}$  events.

and ZEPLIN among others) simultaneously employ the liquid and gas phases of the target material and are designed to detect two signal channels of ultraviolet light. Figure 3 shows the signal channels created by a recoiling nucleus. The primary signal originates from the release of scintillation light by excimers created from nuclear recoil. The secondary signal comes from the ionization electrons, which are drifted up towards the surface of the liquid by application of a strong electric field. These electrons are then extracted into the gas region where they are accelerated by a high electric field, producing electroluminescence. Figure 5 shows a diagram of the design of the XENON10 dual-phase detector. The amount of electroluminescence is proportional to the number of electrons. To discriminate between neutron and WIMP recoils and electron or gamma ray recoils, a comparison of the energy deposited in each signal channel is made (Akimov et al.). Experiments show that neutron recoils produce a scintillation signal that is an order of magnitude higher than the ionization signal, whereas in electron and gamma interactions, the signals are comparable (Akimov et al.). However, such a discrimination approach creates several issues when used with a large target mass.

1. Two-phase detectors can have pile-up problems because of long electron drift times and difficulties in correlating scintillation and ionization signals which

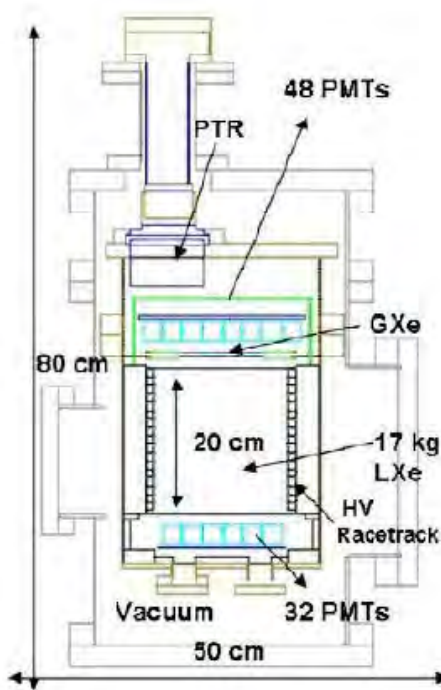


Figure 5: A schematic diagram of the dual-phase XENON10 detector. The photomultiplier tubes, represented by the blue boxes, are stationed below the liquid xenon chamber and above the xenon gas (Saab). PMT coverage is not optimal for such a detector design.

compromises the ability to accurately resolve the position of the WIMP interaction in the detector.

2. Large scale two-phase detectors in the 10-ton range require extremely strong electric fields which must be created by voltages on the order of hundreds of kV.
3. Dual-phase detectors have lower photomultiplier tube (PMT) coverage compared to single phase detectors such as MiniCLEAN. The lower PMT coverage degrades discrimination power, which increases exponentially with light collection.

## 4 MiniCLEAN

The MiniCLEAN experiment circumvents the complications of dual-phase detectors through the utilization of the simpler single phase method to detecting and

discriminating the event signals. The single phase approach immediately eliminates the pile-up concerns and high voltage requirements plaguing dual-phase detectors. Additionally, this detector design allows for the exchange of the target material, a process planned to take place in the MiniCLEAN detector with the exchange of liquid argon by liquid neon. This ability has the advantage of providing a secondary means of signal discrimination through the comparison of the intensity and spectral dependence of signals from the two different targets. The simplicity of the single phase design will also make modeling the detector behavior much more accurate due to the fewer number of parameters needed for simulation.

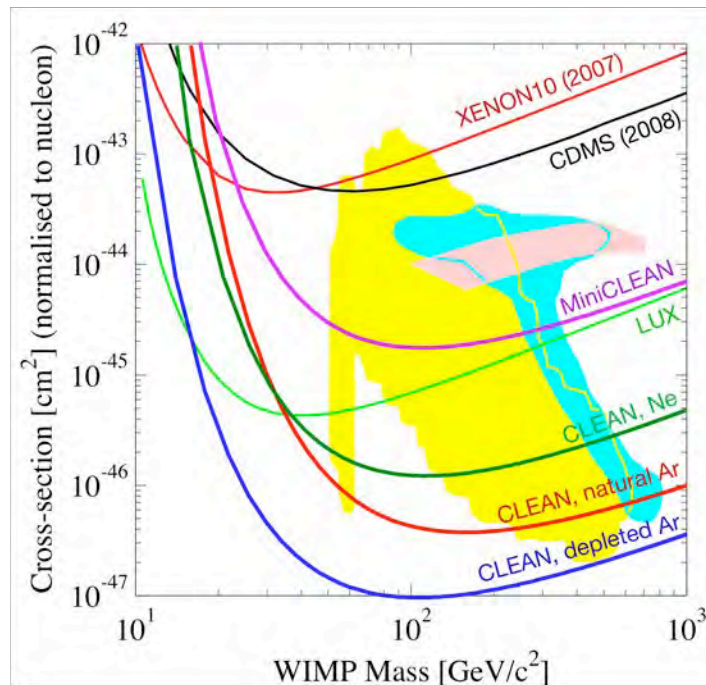


Figure 6: A comparison plot of the upper limits on WIMP mass and cross-section for several dark matter searches. The current best limit is placed by the CDMS detector. The colored regions represent WIMP masses and cross-sections predicted by several models of supersymmetric theory (Courtesy: LANL).

#### 4.1 Goals of the CLEAN Detection Program

The MiniCLEAN detector can be regarded as a concept and design demonstrator for the full scale CLEAN detector. When MiniCLEAN is fully operational it will have sensitivities surpassing all currently running dark matter detection programs.

Figure 6 shows the sensitivities of various dark matter searches. The current best upper limit on the WIMP mass and cross-section is placed by CDMS (Cryogenic Dark Matter Search). Each curve in figure 6 describes the threshold sensitivities for the corresponding detection program. The region above the curve is the exclusion region, which contains WIMP cross-sections and masses that are ruled out by the null results from these experiments. So far, CDMS has had no detection, thus ruling out the region above its curve as possible WIMP cross-sections and masses. However, the majority of theory parameter space (the colored region) remains to be probed and requires sensitivities about three orders of magnitude better than that achieved by CDMS. To achieve such high sensitivities will require present detectors to be scaled up. This, however, is quite a difficult proposition for solid state detectors such as CDMS which uses an expensive supercooled germanium crystal as the target material. MiniCLEAN will not face this difficulty because of the relatively low cost of liquid argon and liquid neon. Once operational, it will be able to probe a large portion of the theory parameter space, and its full-scale follow on, CLEAN, will be able to probe nearly all of parameter space currently predicted by models of supersymmetric theory by utilizing a target mass of  $\sim 100$  tons. The CLEAN detector when filled with neon will also be sensitive to neutrinos from core collapse supernovae and those emanating from our own sun, hence providing science well beyond the search for WIMP dark matter.

## 4.2 Design of MiniCLEAN

As it currently stands, MiniCLEAN will utilize a 400 kg spherical volume of liquid argon as the target for WIMPs. The detector consists of the following primary components: the inner vessel (figure 7), the outer vessel, the optical cassettes (figure 8), and the water shield (figure 9). The inner vessel comprises a stainless steel container which will hold the liquid argon or liquid neon in a 160 cm diameter spherical volume. Surrounding the volume will be 92 9-inch ports and several smaller ports for calibration and cryogen lines; each of the 92 ports will house an optical cassette.

The optical cassette will consist of several distinct components, including the primary steel tube which will hold an 8-inch PMT, a 20 cm long cylindrical acrylic light guide, and a top hat. The front surface of each light guide will be connected to a white acrylic ring whose exact form has not been decided on. The back, concave end will mate the PMT glass surface. The individual optical cassettes will be assembled in a glove box compartment where the acrylic end surfaces are cut away and the remaining piece cleaned to remove any residual radon daughters that might penetrate into the target volume and cause false signals.

Containing the inner vessel and cassette assemblies will be a stainless steel vacuum outer vessel. The primary purpose of the outer vessel is to provide vac-



Figure 7: A cut away view of the MiniCLEAN detector's inner vessel and the surrounding outer vessel. The top hats of the 92 optical cassettes along with the calibration ports are visible.

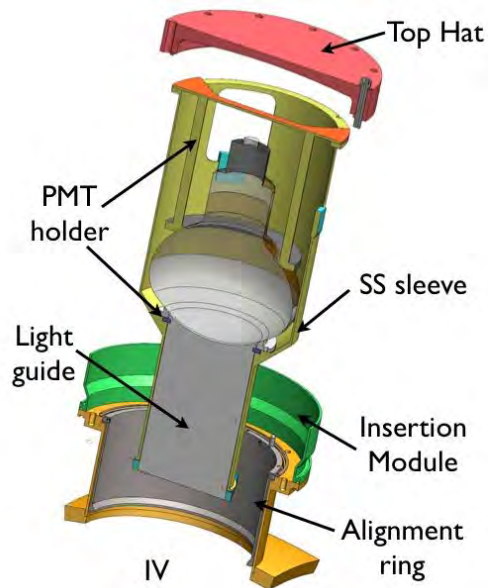


Figure 8: A schematic of the optical cassette design showing the configuration of the acrylic light guide and PMT.

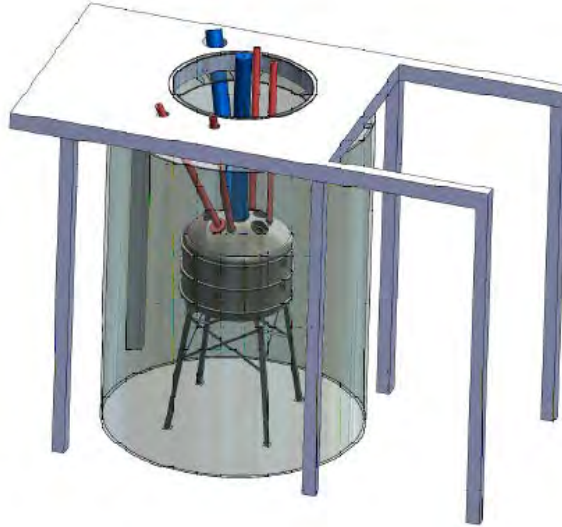


Figure 9: The entire assembly of the MiniCLEAN detector is shown. A large cylindrical water shield tank surrounds the outer vessel supported by struts. The blue and red tubing are calibration and cryogen lines.

uum and thermal insulation so that the inner vessel can be maintained at the temperature of the housed liquid cryogen (87 K for liquid argon and 27 K for liquid neon) and at the same time allow the water shield tank surrounding the outer vessel to be at room temperature. This water shield tank will consist of a cylindrical vessel measuring 18'5" in diameter and 25'11" in height and will serve as an external background rejecter.

### 4.3 Backgrounds

One of the major challenges for MiniCLEAN as well as other detection programs is the mitigation of backgrounds. Without the proper implementation of background rejection techniques, background sources are certain to leak into the target volume and initiate false signals that mimic WIMP induced nuclear recoil. Of particular concern are high energy neutrons penetrating into an inadequately shielded target volume. At present, no technique is known to distinguish between WIMP induced scintillation light and neutron induced scintillation light in noble liquid detectors. The pulse shape discrimination method employed by MiniCLEAN will only allow for the differentiation of neutron and WIMP recoils from electron recoils, and the directionality method employed by another class of detectors (e.g. DRIFT),

which provide a WIMP signature, are not applicable to MiniCLEAN.

### 4.3.1 Cosmic-Ray Induced Neutrons

Neutron backgrounds originate from a variety of sources; among these are cosmic-ray interactions, radioactivity from rocks in the underground chamber housing the detector, and radioactivity in the materials of the detector. To combat external and non-local background sources (i.e. neutrons from cosmic-ray muon interactions), the MiniCLEAN detector will be housed in a deep underground chamber in SNOLAB, a facility located approximately 2 km below the surface in Sudbury Ontario, Canada. Because the composition of the overlying rock varies with location, the depth and shielding effectiveness of these underground facilities are usually given in units called meters water equivalent (m.w.e.) (Saab). The depths and shielding effectiveness of eight different underground laboratories is shown in figure 10. SNOLAB will, in fact, provide some of the best shielding from energetic neutrons created by the interactions of cosmic-ray muons with materials near the detector location.

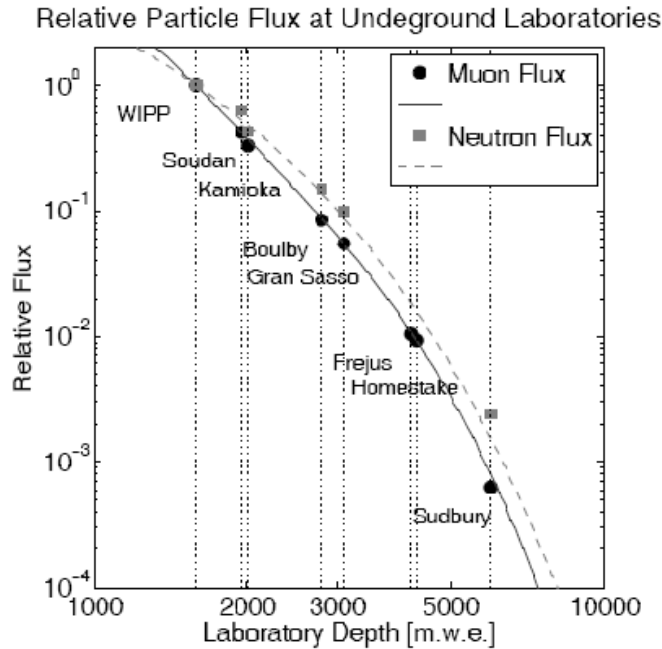


Figure 10: The depths of several underground laboratories in units of m.w.e. with corresponding muon and neutron fluxes. The circles representing muon data are actual measured values. The neutron flux indicated by square boxes and the dashed line are based on a Monte-Carlo simulation (Saab).

### 4.3.2 Local Sources of Backgrounds

Local sources of background, mainly neutrons from the decay chain of uranium and thorium, present other technical challenges. These sources are both external (rocks, external detector parts, etc.) and internal (the containment vessel, electronic components, and other insufficiently radiopure detector parts) to the detector (DMSAG). The water shield tank provides some protection against these sources as well as muon-induced neutrons but is incapable of rejecting background sources internal to the detector. Fiducialization, the process in which the outer portion of the detector volume is also used as a shield to protect the central volume from backgrounds, increases background rejection capabilities, but is still inadequate without employing additional measures to combat radioactivity proximal to the target material.

Unfortunately, the glass of the photomultiplier tubes (PMTs), which are internal to the detector and are used to detect the scintillation light, contain low levels of radioactivity sufficient to produce a significant neutron background and, therefore, cannot be placed too close to the liquid argon. Although progress is being made in producing glass with lower levels of radioactivity, PMTs will still be the dominant neutron source given their close proximity to the target volume. Even for PMTs made with low radioactive glass (1 ppb U), the rate of neutron emission by  $(\alpha, n)$  reactions would still be  $\sim 4$  n/kg/yr (DMSAG). If no additional shielding mechanisms are employed, radioactive particles from the PMTs will undoubtedly leak into the argon and initiate interactions that could produce false signal detections. This is the reason acrylic rods are placed between the PMTs and the liquid argon inner detector in MiniCLEAN. Acrylic has been found to contain levels of U and Th well below 1 part per trillion and is six times more effective at attenuating neutrons than liquid argon alone. However, the UV scintillation light cannot penetrate the acrylic rods, so the acrylic surface in contact with the liquid argon is coated with tetraphenyl butadiene (TPB), a wavelength shifter that converts the liquid argon scintillation light (128 nm) into the visible, which can travel through the acrylic rod to the PMT. The emission and excitation spectrum for TPB is shown in figure 11. In this way, the acrylic rods serve as both shielding of the argon from the radioactivity originating from the PMTs (or other materials in the outer detector), and as light guides to channel the wavelength-shifted scintillation light to the PMTs.

## 5 Acrylic Attenuation

The original work in this honors project centers on the use of the acrylic rods as light guides. Because these acrylic rods will be used as light guides for visible light, it is important to measure the attenuation in acrylic at various wavelengths

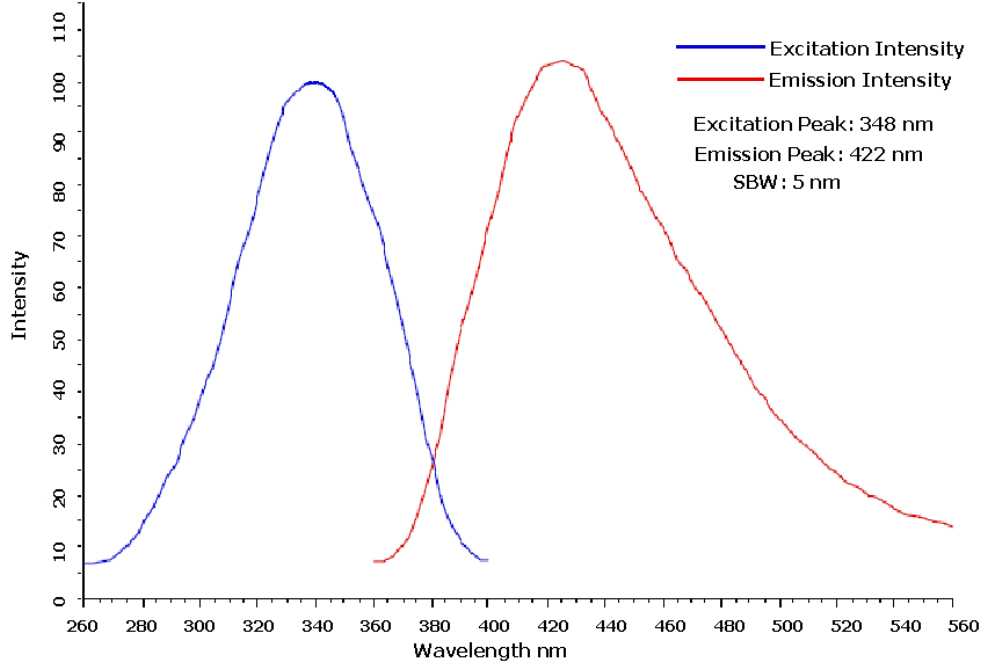


Figure 11: The emission and excitation spectra of TPB with data points recorded at 0.5 nm intervals. The peak emission and excitation wavelengths are 422 nm and 348 nm, respectively [20].

spanning the range produced by the TPB. Since the re-emittance of visible light by TPB is isotropic, the path length that the light travels to the photomultiplier tubes (PMTs) could be many times the length of the acrylic rod (20 cm). Thus, it is critical to know the attenuation of visible light in acrylic precisely, for it would tell us the amount of light that will be detected as a function of energy released in a scintillation event. The distribution of light among the PMTs can be used to determine the origin of the event and this is more accurate the more light is observed. It is essential to be able to determine where inside the detector the event originated in order to discriminate whether the event is the result of a WIMP interaction or an interaction caused by a background neutron, which is likely to occur close to the edges of the detector as opposed to within the fiducial volume.

## 5.1 Definitions

The definition of attenuation is given in the following way: If  $I_0$  is the intensity of the light source and  $I$  is the intensity reaching the detector through a medium of length,  $d$ , then

$$I = I_0 e^{-d/\lambda},$$

where  $\lambda$  is defined as the attenuation length and  $\alpha = 1/\lambda$  is defined as the attenuation coefficient. The determination of the attenuation length allows us to also determine the transmittance. For normal incidence, the internal (i.e. bulk) transmittance is defined by the following relationship,

$$T = e^{-\alpha d},$$

where  $\alpha$  is the absorption coefficient and  $d$  is the length of the acrylic rod.

## 5.2 Previous Acrylic Measurements

Despite the use of acrylic in previous large-scale scintillation detectors (e.g. Sudbury Neutrino Observatory (SNO)), the exact attenuation of visible light in acrylic has not been precisely measured. Previous measurements examined short lengths of acrylic (several cm in length) to determine an average attenuation length that is over a meter long, thus, providing results that are inaccurate, particularly at long wavelengths. These previous measurements were acceptable for uses of several cm of acrylic but not for the current MiniCLEAN experiment that proposes using a 20 cm long acrylic light guide and needs to detect as much light per event as possible. Below, I review the results of studies on the optical properties of acrylic conducted by SNO and the Daya Bay Neutrino Experiment.

### 5.2.1 SNO

The SNO detector, located in deep underground in Sudbury, Ontario, is designed to look for Cherenkov radiation resulting from the interaction of solar neutrinos with  $D_2O$ . A large volume of  $D_2O$  is contained in a large acrylic vessel with a thickness of 5 cm (Zwinkels et al.). Similar to dark matter detectors, precise knowledge of the attenuation of the interaction signal is needed to provide good event reconstruction. The SNO acrylic attenuation measurements were performed on several samples of Polycast acrylic panels (Duncan). The results show that the transmittance of the sample depends on its orientation, perhaps due to surface effects or internal non-uniformities (Duncan). Also, the measurements indicated variations in the attenuation from panel to panel (Duncan). This effect is possibly due to the acrylic manufacturing process and is an effect seen in the measurements performed in this work. Figure 12 shows the transmittance curves for three samples of acrylic used in the SNO measurements.

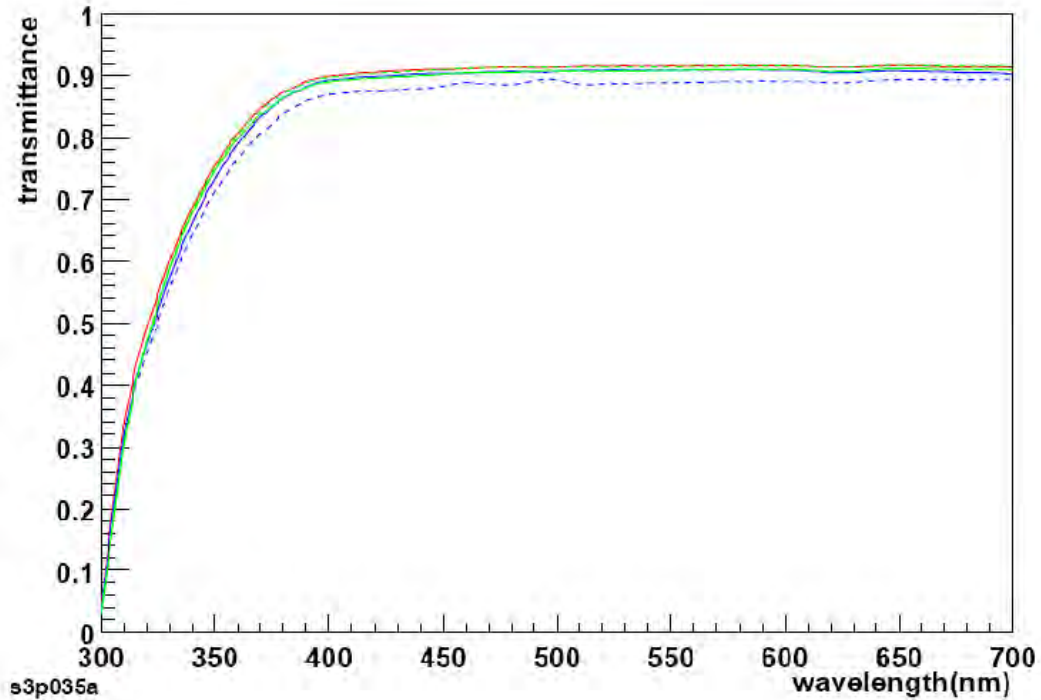


Figure 12: The transmittance curves for three samples of acrylic measured by SNO. There are five curves plotted here. The dashed blue and green curves represent the same two samples that had been rotated by 90 degrees.

### 5.2.2 Daya Bay

The Daya Bay reactor neutrino experiment is a neutrino oscillation experiment designed to study anti-neutrinos produced by the Daya Bay Nuclear Complex, a facility located in southern China (Cao). The detector will utilize a cylindrical acrylic tank to house a liquid target scintillator (Pun). As part of this experiment, measurements of the transmittance of several acrylic samples approximately 1.2 cm wide and 5.5 cm tall were conducted using a spectrophotometer. The transmittance was measured for a UVT acrylic sheet from Polycast and a UVT acrylic block from Reynolds. The measuring pathlengths (distances traveled by light through the acrylic sample) ranged from 12 mm to 60 mm. Their results showed a relatively flat transmission level between 400 nm and 850 nm with a sharp drop off between 300 nm and 400 nm. Interestingly, the results also showed that the transmission curve was not entirely consistent for the same sample of acrylic measured with different pathlengths. These results have not yet been published and was obtained through private communications with Bryce Littlejohn.

### 5.3 Acrylic Samples

Samples of UV transparent acrylic rods of varying lengths (up to 2.5 m in length) and diameters (5-20 cm) were acquired from three different manufacturers: Spartech Polycast, Rohm (extruded by Plastifab), and Reynolds Polymer Technology (RPT). A total of 8 samples were obtained for measurements. From Spartech, two 20 cm rods and one 5 cm rod were obtained. From Rohm, two 20 cm rods were obtained. Three 12 cm rods were also obtained from RPT.

### 5.4 Experimental Setup

The goal of this project was to obtain accurate attenuation measurements of acrylic through a simple experimental setup. Each acrylic rod was sequentially placed between a laser and a Newport photo-detector (Model 918-UV) sensitive to the wavelength range of the lasers used in the experiment, and the light intensity was measured both with and without the acrylic. The intensity readings were provided by a Newport power meter (Model 1930C), and a comparison of the reading made with the acrylic rod and without the acrylic allowed us to determine the attenuation. Before measurements were made, the rods were all cut down to approximately 92 cm in length and both end surfaces were polished by the UNM Physics Department machine shop. The exact length of each rod was then individually measured. Initial plans to carry out measurements on longer samples of acrylic were put aside because of the difficulty in aligning the rod for detection and the inability to find an optical bench long enough to accommodate the longer rods.

These measurements were conducted with solid state diode lasers at 440 nm (Model LDCU12/6415), 405 nm (Model PPMT 50), and 375 nm (Model PPMT 16) produced by Power Technology and two helium-neon gas lasers at 543 nm (Model LHGR-0050) and 632 nm (Model 155) produced by PMS Electro-Optics and Spectra-Physics, respectively. An apparatus was also constructed to rotate the rods and allow a series of measurements to be made on each rod to test the uniformity of the acrylic. Figure 13 is a diagram of the basic setup for the experiment, excluding the apparatus that was used to rotate the rods.

In addition, a 2 inch refocusing lens was positioned between the photo-detector and the acrylic rod to refocus the light prior to detection. The dispersion of the beam in a very long rod often caused the size of the beam to be larger than the detector area of the photo-detector. Also, surface irregularities resulting from the polishing process could also contribute to the dispersion of the laser beam.

Before measurements were conducted, great effort was taken in carefully aligning the laser, rod, and photo-detector so that the incident laser beam was normal to the acrylic surface. Because of the dissimilar index of refraction of air and

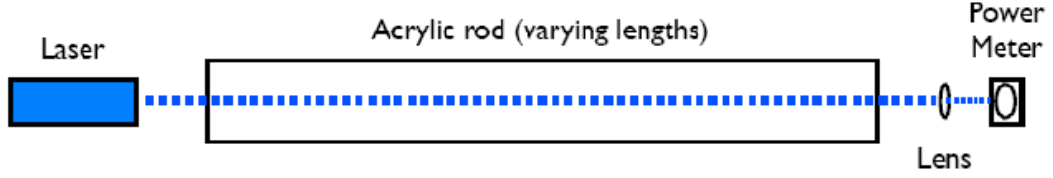


Figure 13: A diagram of the basic setup of the experiment. The roller assembly is not shown here.

acrylic, a fraction of the light is expected to be lost by reflection at each of the end surfaces. By applying the electromagnetic boundary conditions on the acrylic-air interface, the ratio of the electric field amplitudes are found to be

$$\frac{E_R}{E_I} = \left| \frac{n_1 - n_2}{n_1 + n_2} \right|,$$

where  $E_R$  is the reflected electric field amplitude and  $E_I$  is the incident electric field amplitude, and  $n_1$  and  $n_2$  represent the indices of refraction for acrylic and air, respectively (Griffiths). If we assume a complex index of refraction given by

$$\tilde{n} = n + i\kappa,$$

where  $n$  is the usual index of refraction defined as  $n = v/c$  and  $\kappa$  is the absorption index and is related to the attenuation coefficient by  $\alpha = 4\pi\kappa/\lambda$ , and use the definition of reflectance, which is the following:

$$R = \frac{I_R}{I_I} = \left( \frac{E_R}{E_I} \right)^2,$$

then the reflectance is

$$R = \frac{(n - 1)^2 + \kappa^2}{(n + 1)^2 + \kappa^2}.$$

Here, the index of refraction for air is taken to be unity, with no complex component. Because the attenuation length is on the order of 10's to 100's of cm and the wavelength of the laser light is on the order of 100 nm,  $\kappa$  is  $\ll 1$  and can be ignored. Inserting a value of approximately 1.50 for the measured index of refraction of acrylic, we find that 4% of the incident light is reflected at the first interface. Similarly, 4% of the attenuated incident light will be reflected at the second interface. The actual fraction of incident, non-attenuated light reflected at the second surface was calculated from the measurements of the light intensities with and without the acrylic rod in place. The fraction is dependent on the

Total Reflectance, $R$					
Wavelength (nm)	375	405	440	543	632
Spartech 1	0.050	0.057	0.061	0.067	0.071
Spartech 2	0.049	0.057	0.061	0.066	0.071
Spartech 3	0.048	0.066	0.070	0.073	0.076
Rohm 1	0.040	0.048	0.074	0.075	0.077
Rohm 2	0.040	0.043	0.062	0.068	0.075
RPT 1	0.043	0.061	0.066	0.071	0.075
RPT 2	0.043	0.060	0.065	0.070	0.074
RPT 3	0.043	0.062	0.067	0.070	0.075

Table 2: The total reflectance for all samples of acrylic at the wavelengths measured in the experiment. These values were derived from measurements made with the refocusing lens.

attenuation length, and consequently varies from rod to rod and is wavelength dependent. Table 2 gives the total reflectance for each rod at the wavelengths considered in this experiment and is derived from measurements taken with the refocusing lens.

## 5.5 Experimental Procedure

The procedure for conducting the measurements was the following: A sample of the acrylic rod is placed on the roller assembly. The assembly is first moved out of the path of the laser beam. The photo-detector is carefully adjusted via an X-Y stage to allow the beam to strike its center and a measurement of the laser’s power was recorded. The refocusing lens was then placed in the beam path and its position was slowly adjusted to give the maximum reading on the power meter. The maximum reading was then recorded. The assembly is then positioned in the path of the beam such that beam is incident approximately midway between the center and edge of the rod to allow for measurements to be made at different positions when the rod is rotated. The laser, acrylic assembly, and detector are then aligned so that the beam is normally incident on the acrylic surface and strikes the center of the photo-detector. A measurement was then taken of the attenuated beam with and without the refocusing lens and a marker was placed on the acrylic rod to mark the position of the first measurement. The rod was then subsequently rotated by 90 degrees and a measurement was made at this position. The process was repeated two more times to obtain a total of eight measurements (four without the lens and four with the lens) at equally spaced

440 nm Measurements						
Set	no acrylic ( $\mu W$ )	w/acrylic ( $\mu W$ )				
#1	80.0	33.0	31.9	30.0	27.4	
#2	79.6	33.2	31.5	28.9	28.0	
#3	79.4	33.0	30.9	29.0	27.7	

Table 3: A sample of the power measurements in units of microwatts for Sparteck sample 1 at 440 nm. These measurements were made without the refocusing lens, but similar sets of measurements are also performed with the refocusing lens. Each row corresponds to one set of measurements. The last four measurements in each row were made at four equally separated positions on the rod.

positions around the rod.

After this set of measurements, the acrylic assembly was removed from the laser beam path and a measurement was made on the non-attenuated beam both with and without the refocusing lens as a check for any power instabilities in the laser. Once again, the acrylic assembly was repositioned in the beam path and eight measurements were made at the same positions measured in the first series. This procedure was then repeated for a third and final time. In all, twenty-four measurements (12 with the refocusing lens and 12 without) of the attenuated laser beam were made and six (3 with the lens and 3 without) were made for the non-attenuated beam. The rod is then removed from the roller and another rod is inserted. The same process is repeated for this second rod and the other six rods at all five wavelengths. Table 3 is a sample of the measurements made for one rod at one particular wavelength without the refocusing lens. A similar set of measurements was also made with the refocusing lens.

A complete set of measurements for one rod at one wavelength of light took approximately one hour. The entire measurements for all eight rods at all five wavelengths are estimated to have taken 50 hours. The extra 10 hours are due to the time needed to change the lasers and allow them to warm up before measurements were made. For the solid state lasers, the warm up time was 15 minutes. For the 543 nm helium-neon laser, the warm up time was considerably longer, about 2 hours. For the 632 nm helium-neon laser, the warm up time was 30 minutes. These warm up times were determined by monitoring the power meter and waiting until the reading stabilized before proceeding to make measurements. It was found that the helium-neon lasers were much more unstable than the three solid state lasers. Power fluctuations of the 543 nm laser were about 3% and about 7% for the 632 nm laser. The solid state lasers had fluctuations of about

1%. Because of these instabilities, the average of the maximum and minimum power readings was recorded for each measurement.

During the measuring process, the ambient light from the room lights was blocked by draping a dark cloth over the entire measuring apparatus (laser, rod, and photo-detector) for all of the wavelengths in which the attenuation was measured, except for the 375 nm measurements. Measurements made with the 375 nm laser were done with the lights off because it was very difficult to find the beam exiting the acrylic rod for purposes of aligning it with the photo-detector under ambient lighting conditions. This was not done at the longer wavelengths because the lab containing the experimental setup was concurrently used by other people. The cloth blocked most of the external light but allowed a small amount (a few tenths of a microwatt) to leak through.

## 5.6 Systematic Uncertainties

The uncertainties in the attenuation measurements were evaluated once all measurements were completed. One of the sources of uncertainties resulted from the imperfect blockage of ambient light by the cloth, so a single measurement was made for each rod at each wavelength with the ambient lights turned off and with the lights on and the cloth covering draped over the setup. These measurements were made both with and without the refocusing lens. The error was simply determined by comparing these measurements to those made with the cloth covering and the lights on. These measurements were only made for the 405 nm and 440 nm lasers due to the fact that the power fluctuations of the 543 nm and 632 nm lasers were much higher than the differences between the readings made with and without the lights. However, it was found that the uncertainty introduced by the lighting was essentially negligible, contributing less than a 1% error to the ratio of attenuated power to un-attenuated power.

The second source of uncertainty was due to the laser power instability. This uncertainty was calculated by first taking the ratio of the attenuated power to the un-attenuated power for all four positions in the first set of measurements, and this was then repeated for the second and third sets. Then, the standard deviation of those three ratios corresponding to the same position was calculated. This calculation was repeated for the other three positions. The percent uncertainty in the ratio was found by taking the ratio of the standard deviation to the average of the power ratio for each position separately. Then an average of the percent uncertainties was taken. These calculations were performed for each rod at each wavelength and for the two cases in which the measurements were made; the case with the refocusing lens and the case without the refocusing lens.

The final uncertainty considered was a position-related uncertainty due to the possible internal non-uniformity of the rods as well as end surface effects. First,

an average of the three un-attenuated power measurements was taken. Then, an average of the attenuated power measurements at the same position was calculated for all four positions, separately. Next, the ratio of the average attenuated power to the average un-attenuated power at each position was taken. Finally, the standard deviation of these four ratios was calculated, and a ratio of this value to the average of the power ratios was taken to find the percent uncertainty. The total error due to all three sources was obtained by adding the errors in quadrature.

## 5.7 Results

Once the total error in the measurements was determined, the attenuation lengths were determined by inverting the attenuation equation and solving for  $\lambda$ . The length,  $d$ , was measured for each rod, and the average values of  $I$  and  $I_0$  at each wavelength were taken to calculate the attenuation length.  $I_0$  was taken to be  $(1 - R)I_0$ , where  $R$  is the total reflectance due to both end surfaces. Tables 4-9 list the attenuation lengths for all samples of acrylic rods measured in this experiment. Because the attenuation length error bars are non-symmetric, they are not including in these tables but will be shown in the transmittance tables instead. Except for Spartech sample 2 in which the dispersive effect of the end surfaces was most pronounced, the attenuation lengths and transmittances of the other samples at 632 nm are the same for both the lens/no lens case because the differences between the power readings in the two cases were much smaller than the power fluctuations in laser power. To aid in the interpretation of the data, plots of the attenuation lengths as a function of wavelength were created. However, since the attenuation lengths span such a wide range and because the plots were dominated by the 632 nm measurements, the bulk transmittances of the acrylic rods as a function of wavelength are presented here instead. As a way to compare samples made by different manufacturers, the bulk transmittance through one meter of acrylic is calculated and presented.

Spartech Attenuation Lengths (cm): No Lens					
Wavelength (nm)	375	405	440	543	632
Spartech 1	51.2	85.0	101.9	205.1	400.5
Spartech 2	46.2	73.3	87.9	116.7	248.5
Spartech 3	47.6	168.0	217.0	612.7	1713.3

Table 4: The attenuation lengths for three samples of Spartech acrylic. Samples 1 and 2 are 20 cm in diameter while sample three is 5 cm in diameter. These lengths were derived from measurements made without the refocusing lens and show a large difference between the attenuation lengths of sample 3 and samples 1 and 2.

Spartech Attenuation Lengths (cm): With Lens					
Wavelength (nm)	375	405	440	543	632
Spartech 1	65.4	113.1	146.3	240.7	400.5
Spartech 2	62.4	107.6	144.9	221.6	432.4
Spartech 3	55.4	223.2	352.8	568.6	1713.3

Table 5: The attenuation lengths of three samples of Spartech acrylic as derived from measurements made with the refocusing lens. The attenuation lengths for samples 1 and 2 here are more consistent than the attenuation lengths calculated from measurements made without the refocusing lens, but the large deviation of the attenuation lengths of sample 3 from samples 1 and 2 is still present.

Rohm Attenuation Lengths (cm): No Lens					
Wavelength (nm)	375	405	440	543	632
Rohm 1	–	55.5	511.6	1288.9	2074.8
Rohm 2	–	34.9	155.8	313.2	954.6

Table 6: The attenuation lengths for two samples of Rohm acrylic, both having the same diameter (20 cm). No readings (detections) were made without the refocusing lens at 375 nm. The inconsistency of the two samples is evident. Both samples displayed a large increase in the attenuation length from 405 nm to 440 nm, suggesting the acrylic is UVA rather than UVT.

Rohm Attenuation Lengths (cm): With Lens					
Wavelength (nm)	375	405	440	543	632
Rohm 1	12.3	55.5	751.7	989.7	2074.8
Rohm 2	10.2	34.9	162.6	285.6	954.6

Table 7: The attenuation lengths for two samples of Rohm acrylic, both having the same diameter (20 cm). Readings were made with the refocusing lens at 375 nm, suggesting dispersion due to the end surfaces as the reason for the non-detection in the case without the refocusing lens.

RPT Attenuation Lengths (cm): No Lens					
Wavelength (nm)	375	405	440	543	632
RPT 1	31.3	131.5	197.3	360.4	879.3
RPT 2	31.6	120.3	171.5	323.6	686.9
RPT 3	30.2	130.9	192.3	350.8	1043.7

Table 8: The attenuation lengths for three samples of RPT acrylic of the same diameter (20 cm) derived from measurements without the refocusing lens. In contrast to the Spartech and Rohm acrylic rods, samples from RPT show more consistency in the attenuation lengths across different samples.

RPT Attenuation Lengths (cm): With Lens					
Wavelength (nm)	375	405	440	543	632
RPT 1	35.3	146.8	232.1	401.3	879.3
RPT 2	35.7	139.2	216.7	344.5	686.9
RPT 3	33.3	154.2	263.0	367.7	1043.7

Table 9: The attenuation lengths for three samples of RPT acrylic of the same diameter (20 cm) derived from measurements made with the refocusing lens.

## 5.8 Discussion

The most noticeable results from measurements on the Spartech samples are the significant differences between the transmittance values derived from measurements taken with and without the refocusing lens, specifically in the case of Spartech samples 1 & 2. This result was, indeed, anticipated because the large

dispersion of the attenuated beam was clearly perceptible during the measuring process and is the result of deficiencies in the polishing of the end surfaces. Much effort was given to adjusting the lens to obtain the maximal power reading. Although the recorded power measurements were considerably higher with the refocusing lens, the efficiency of the lens to refocus the light prior to detection is not entirely clear without measurements being conducted on these same samples with better polished end surfaces. However, the most interesting result is the unexpected large discrepancy between the transmittances of Spartech sample 3 (5 cm diameter) and samples 1 & 2 (both 20 cm in diameter). A possible explanation is that sample 3 is a different grade of acrylic from samples 1 & 2 and so the chemical composition is not identical. The manufacturer was contacted to help explain the finding and possibly verify or dismiss that hypothesis. In fact, they explained to us that the three samples were all similar in composition and that the discrepancy might be due to contamination. This does not seem entirely convincing since no evidence of contamination was visible. Another possible explanation could be that the optical properties of the acrylic rods are dependent on the details of their processing histories, particularly how the acrylic is formed into rods. This information is, however, proprietary and was not made available to us.

Spartech Transmittance (%): No Lens			
Wavelength (nm)	Spartech 1	Spartech 2	Spartech 3
375	$14.2 \pm 0.5$	$11.5 \pm 0.4$	$12.3 \pm 0.1$
405	$30.9 \pm 1.7$	$25.6 \pm 1.2$	$55.2 \pm 0.4$
440	$37.5 \pm 3.2$	$32.1 \pm 1.8$	$63.1 \pm 0.7$
543	$61.4 \pm 3.4$	$42.4 \pm 3.4$	$84.9 \pm 1.6$
632	$77.9 \pm 4.7$	$66.9 \pm 6.5$	$94.3 \pm 0.8$

Table 10: The transmittances of three samples of Spartech acrylic through 1 meter as derived from measurements made without the refocusing lens. The relatively large errors in the transmittance levels for samples 1 and 2 at the longer wavelengths are primarily due to inadequate polishing of the end surfaces of the rods which can be seen by comparison with the values for the case with the refocusing lens.

In contrast to the Spartech samples, there is minimal deviation in the transmittance values of the Rohm acrylic samples as derived from the measurements made with the refocusing lens and without the refocusing lens. This points to a better polishing of the end surfaces of the acrylic rods. Another noticeable observation is the large difference in the transmittances of the two samples at the

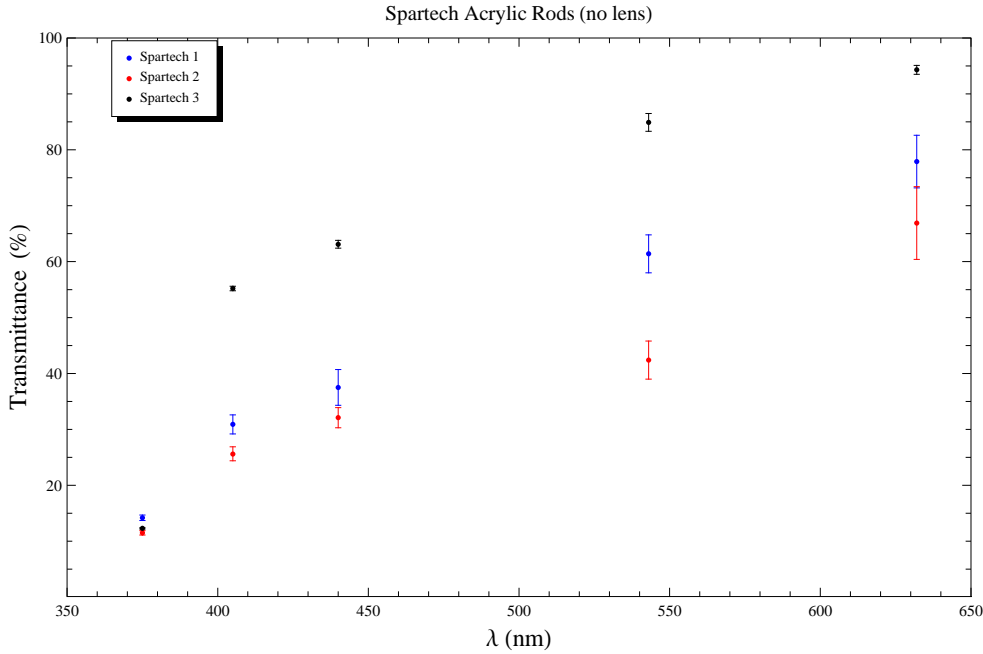


Figure 14: A plot of the transmittance as a function of wavelength for three samples of Spartech acrylic rods as derived from measurements without the refocusing lens.

Spartech Transmittance (%): With Lens			
Wavelength (nm)	Spartech 1	Spartech 2	Spartech 3
375	$21.7 \pm 0.5$	$20.1 \pm 0.5$	$16.5 \pm 0.2$
405	$41.3 \pm 1.5$	$39.5 \pm 0.8$	$63.9 \pm 0.8$
440	$50.5 \pm 3.0$	$50.2 \pm 1.5$	$75.3 \pm 0.7$
543	$66.0 \pm 3.4$	$63.7 \pm 1.6$	$83.9 \pm 1.6$
632	$77.9 \pm 4.7$	$79.4 \pm 0.8$	$94.3 \pm 0.8$

Table 11: The transmittances of three samples of Spartech acrylic through 1 meter as derived from measurements made with the refocusing lens. Samples 1 and 2, both 20 cm in diameter, have very similar transmittance levels, but both vary from the 5 cm sample 3.

three intermediate wavelengths (405 nm, 440nm, and 543 nm). Again, this discrepancy could be due to the forming process which causes inconsistencies in the optical properties of the acrylic from rod to rod or from batch to batch. Beside the disparity in the transmittance observed from rod to rod, there is an interest-

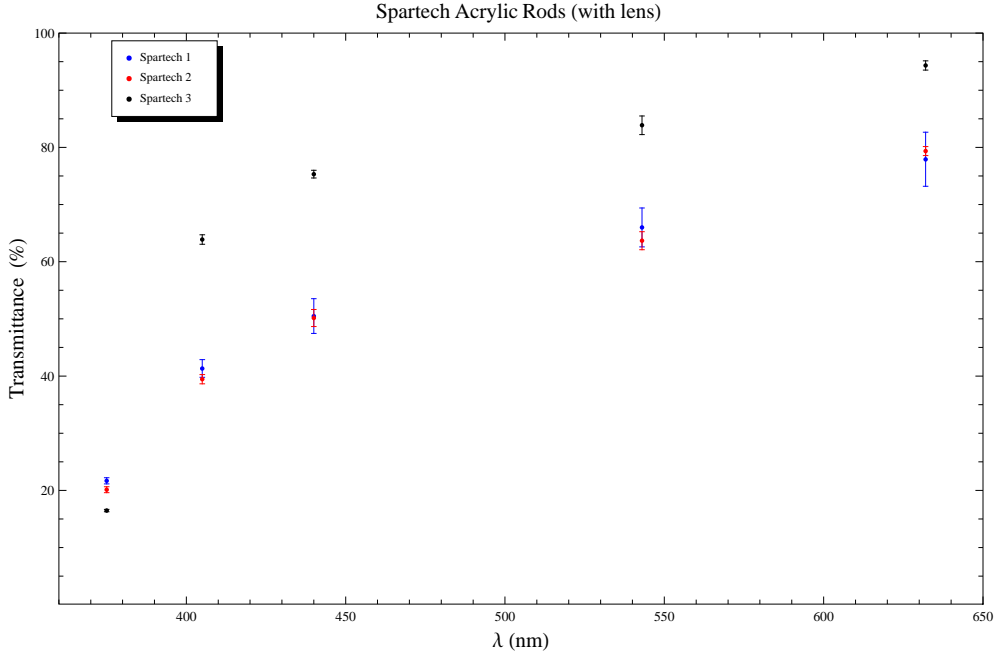


Figure 15: A plot of the transmittance as a function of wavelength for three samples of Spartech acrylic rods as derived from measurements made with the refocusing lens. The transmittances of Spartech samples 1 and 2 are much more consistent, indicating dispersive effects due to the end surfaces.

ing behavior in each rod separately. The Rohm acrylic rods have essentially zero transmittance at 375 nm and a sharp drop in the transmittance from 440 nm to 405 nm. These two features are quite different from the Spartech samples and suggest that the samples might not be ultra-violet transmitting (UVT) acrylic but ultra-violet absorbing (UVA) acrylic which transmits over a more limited spectral range. Plastifab, the company that extruded the rods from Rohm acrylic, was able to confirm this suspicion after examining the manufacturing records that these rods were made from material that was a mixture of UVA and some UVT acrylic. This material mixture explains the measured performance at wavelengths below 440 nm. The company is in the process of manufacturing new acrylic rods with material composed completely of UVT acrylic and a significant improvement is expected.

Rohm Transmittance (%): No Lens		
Wavelength (nm)	Rohm 1	Rohm 2
375	--	--
405	$16.5 \pm 0.3$	$5.7 \pm 0.3$
440	$82.2 \pm 1.2$	$52.6 \pm 1.3$
543	$92.5 \pm 2.1$	$72.7 \pm 2.0$
632	$95.3 \pm 2.0$	$90.1 \pm 1.1$

Table 12: The transmittances of two samples of Rohm acrylic through 1 meter as derived from measurements made without the refocusing lens. The difference in the transmittance levels between the two samples were still present even when the refocusing lens was used, suggesting that the end surfaces of the rods are unlikely to be the contributing factor.

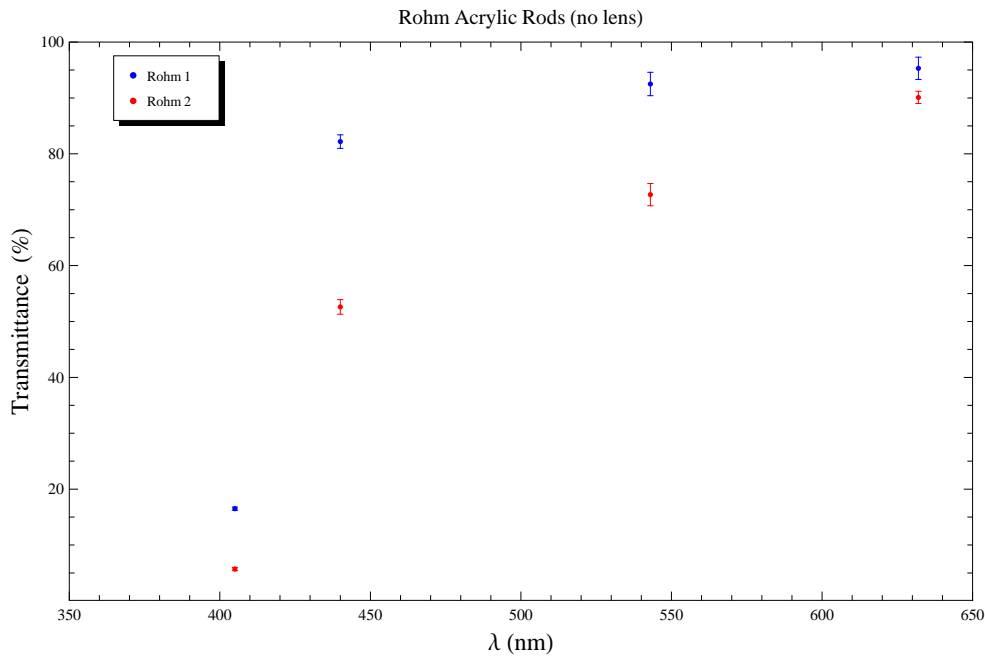


Figure 16: A plot of the transmittance as function of wavelength for two samples of acrylic rods from Rohm. These data points were derived from measurements made without the refocusing lens. The plot shows a large difference in the transmittance of the two samples, particularly at 440 nm and 543 nm. There was no detection at 375 nm, and so the transmittance levels at this wavelength is essentially zero.

Rohm Transmittance (%): With Lens		
Wavelength (nm)	Rohm 1	Rohm 2
375	0.0	0.0
405	$16.5 \pm 0.3$	$5.7 \pm 0.3$
440	$87.5 \pm 1.8$	$54.1 \pm 1.2$
543	$90.4 \pm 1.7$	$70.7 \pm 1.2$
632	$95.3 \pm 2.0$	$90.1 \pm 1.1$

Table 13: The transmittance levels of two samples of Rohm acrylic through 1 meter derived from measurements made with the refocusing lens. Even with the refocusing lens, the transmittance at 375 nm was essentially zero.

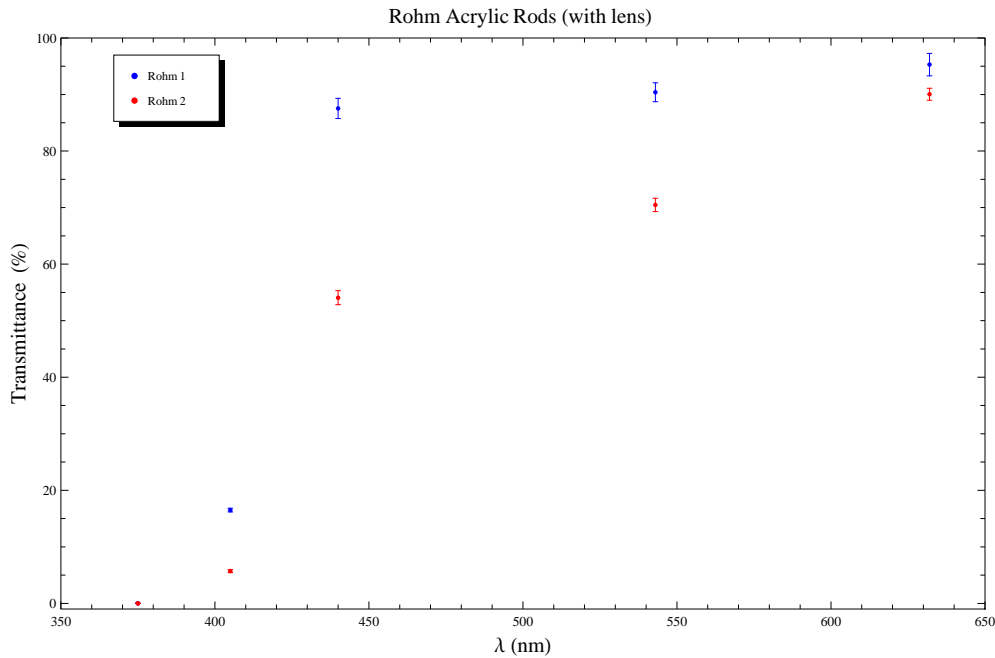


Figure 17: A plot of the transmittance as a function of wavelength for two samples of acrylic rods from Rohm as derived from measurements made with the refocusing lens. The variability in these samples are evident even with the use of the refocusing lens, suggesting that inconsistent internal properties which are likely due to the manufacturing process could be the cause.

The RPT samples exhibited the highest consistency in transmittance levels across all samples at the measured wavelengths. These samples displayed similar performance to the 5 cm diameter Spartech sample 3 but differed from the Rohm

samples in that there is no sharp drop in transmittance from 440 nm to 405 nm, which again shows the characteristically different optical properties for UVT and UVA acrylic.

RPT Transmittance (%): No Lens			
Wavelength (nm)	RPT 1	RPT 2	RPT 3
375	$4.1 \pm 0.3$	$4.2 \pm 0.4$	$3.7 \pm 0.2$
405	$46.7 \pm 0.6$	$43.6 \pm 0.9$	$46.6 \pm 1.5$
440	$60.2 \pm 0.9$	$55.8 \pm 0.5$	$59.5 \pm 1.0$
543	$75.8 \pm 1.7$	$73.4 \pm 1.3$	$75.2 \pm 0.9$
632	$89.3 \pm 2.3$	$86.5 \pm 2.2$	$90.9 \pm 2.4$

Table 14: The transmittances of three samples of RPT acrylic through 1 meter as derived from measurements made without the refocusing lens.

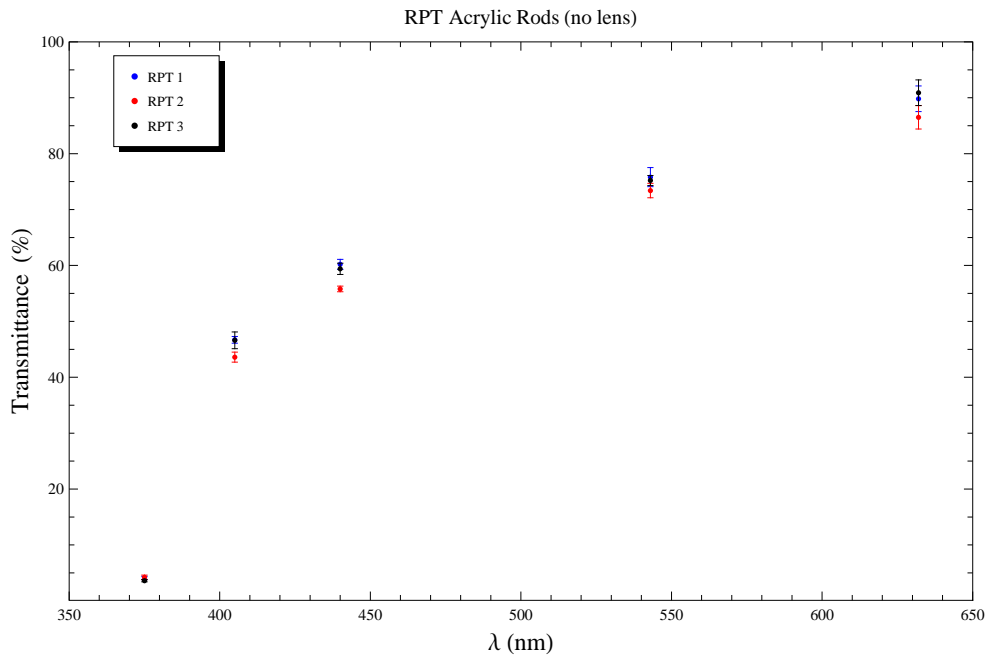


Figure 18: A plot of the transmittance for three samples of acrylic rods from RPT. The transmittance of these rods are highly consistent with each other even without the use of the refocusing lens. This is in contrast to the Sparteck and Rohm samples which had transmittance levels that were highly variable from sample to sample.

RPT Transmittance (%): With Lens			
Wavelength (nm)	RPT 1	RPT 2	RPT 3
375	$5.9 \pm 0.4$	$6.1 \pm 0.4$	$5.0 \pm 0.3$
405	$50.6 \pm 0.5$	$48.8 \pm 0.9$	$52.3 \pm 1.1$
440	$65.0 \pm 0.9$	$63.0 \pm 2.0$	$68.4 \pm 0.8$
543	$77.9 \pm 1.7$	$74.8 \pm 1.8$	$76.2 \pm 0.7$
632	$89.3 \pm 2.3$	$86.5 \pm 2.1$	$90.9 \pm 2.4$

Table 15: The transmittances of three samples of RPT acrylic through 1 meter derived from measurements made with the refocusing lens.

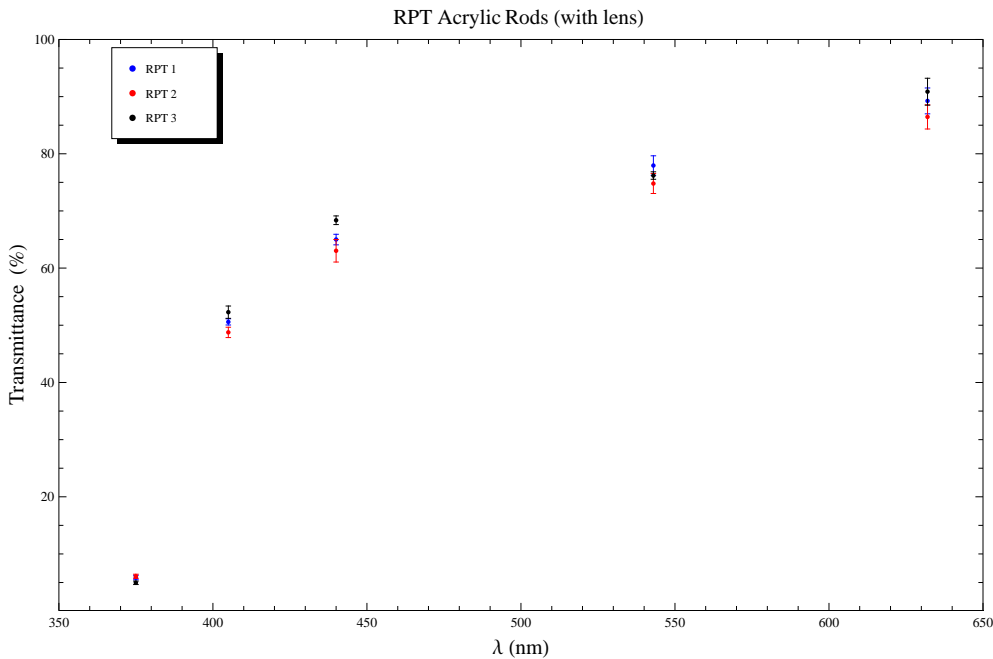


Figure 19: A plot of the transmittance for three samples of acrylic rods from RPT. The consistency of the RPT acrylic samples is still present when the refocusing lens is used.

In addition, a table and plot of the transmittance of the best performing sample from each manufacturer is given. A sample was selected as the best performing sample by its transmittance at 440 nm, which is close to the wavelength of peak emission for TPB. The wavelength dependence of the transmittance of Spartech sample 3 and RPT sample 3 are quite similar even though the Spartech sample has a higher transmittance at each wavelength that was measured. The plot shows

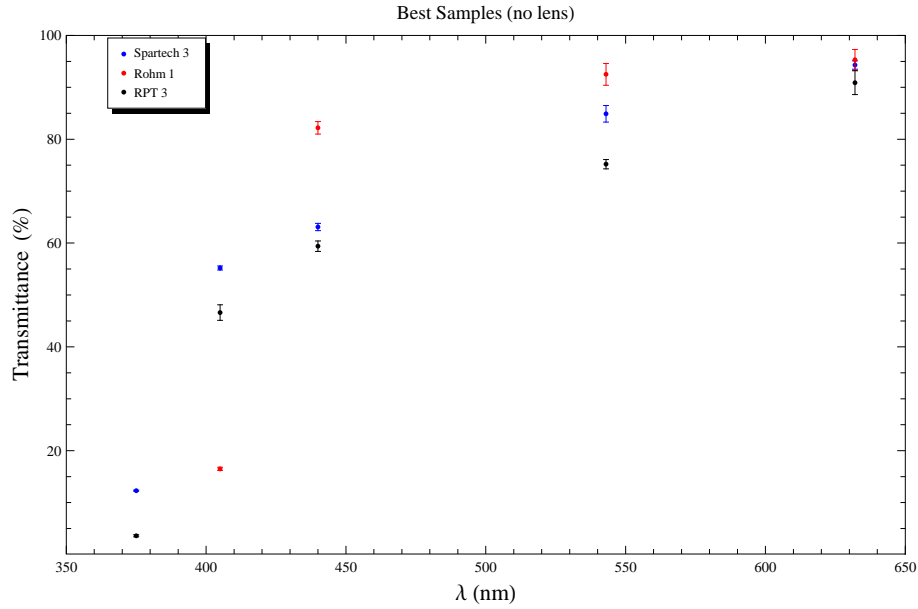


Figure 20: A plot of the transmittance levels of the best three samples of acrylic rods, one from each manufacturer. These data points were derived from measurements made without the refocusing lens.

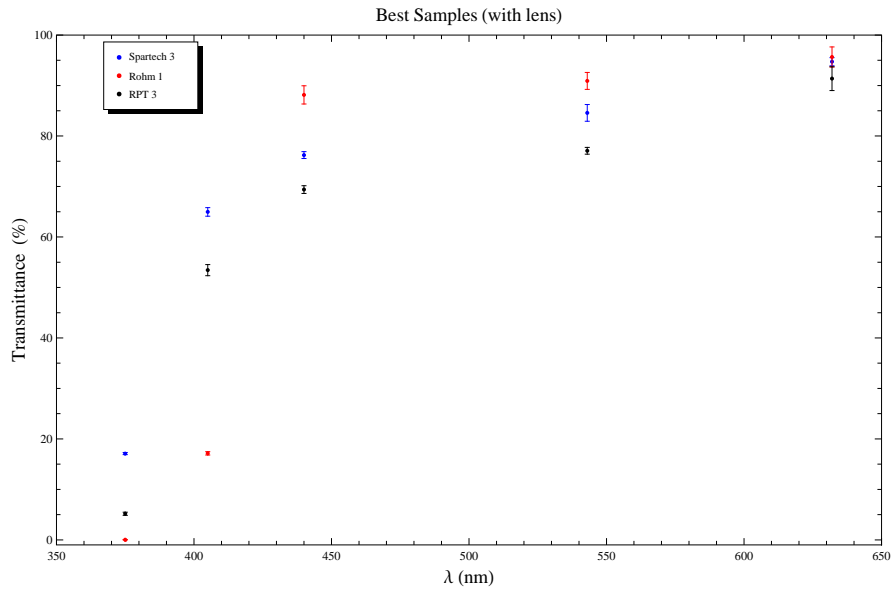


Figure 21: A plot of the transmittance three of the best samples of acrylic rods, one from each manufacturer. These data points were derived measurements were made with the refocusing lens.

the distinctive behavior of the Rohm sample with the sharp drop-off from 440 nm to 405 nm. Although the consistency of the three RPT samples is a favorable characteristic, the lower transmittance levels as compared to the Spartech sample 3 would result in lower light collection from a nuclear-recoil signal, degrading both signal detection and discrimination. Sample 3 from Spartech would serve as a better acrylic for the light guides. However, the light guides in the MiniCLEAN detector will have a larger diameter (20 cm) than the Spartech sample 3 rod (5 cm). This presents a problem since the measured transmittance of the two 20 cm Spartech rods was considerably lower than sample 3. The Rohm sample 1 can also be considered for use as light guide because of its relatively high transmittance at 440 nm, but the inconsistency between rods, specifically with Rohm sample 2 having a lowering transmittance at 440 nm than sample 1 as well as both RPT and Spartech samples 3, also raises a problem.

## 5.9 Conclusions

The measurements of the attenuation of acrylic suggest a high degree of variability in the optical properties of acrylic rods from different manufacturers and even between rods from the same manufacturers, which, perhaps, might be due to different rod manufacturing techniques. Thus, no assumption can be made on the property of the acrylic sample before it is tested. It is recommended that MiniCLEAN perform an evaluation on each acrylic light guide after its manufacture and machining to determine if its optical attenuation is acceptable. Measurements should be performed on each sample at several wavelengths spanning the range emitted by TPB to properly characterize their transmitting behavior. Measurements made at only one wavelength are insufficient to deduce the transmittance of the acrylic over a wide spectral range as can be seen from the large drop off in the transmittance of the samples from Rohm and the relatively smooth change in the transmittance levels for samples from Spartech and RPT between 440 nm and 405 nm. In addition, more attention should be given to polishing the end surfaces of the acrylic, which can have a significant impact on the measurements that are obtained. A similar experimental setup and procedure should be employed for these future measurements and longer rods could be used to obtain more accurate attenuation lengths at wavelengths greater than 440 nm. These measurements would characterize the transmitting behavior of each of the 92 acrylic light guides in the detector and would improve both signal discrimination and the ability to reconstruct the event location, both of which are critical to the success of the MiniCLEAN program.

## 6 Acknowledgments

Great appreciation is owed to the following people without whom this research project could not be completed. Keith Rielage (LANL) and Dinesh Loomba, who have helped me every step of the way, devoted a considerable amount of their time to proofreading the drafts for this paper and have offered helpful comments that have greatly improved it. I would also like to thank John Matthews for his help and allowing me to use his equipment to perform the measurements. Appreciation is also owed to Paul Schwoebel and Wolfgang Rudolf for lending us their lasers, and to John Demoss and his crew at the machine shop for cutting and polishing the acrylic rods and also constructing the roller assembly.

## References

- [1] Bradley W. Carroll and Dale A. Ostlie, *An Introduction to Modern Astrophysics*. Addison Wesley, San Francisco, 2nd Edition, 2007.
- [2] De-Chang Dai, Reijiro Matsuo, Glenn Starkman, arXiv:0806.4319v2 [gr-qc].
- [3] D. Clowe, S. W. Randall, M. Markevitch, arXiv:astro-ph/0611496v1.
- [4] David B. Cline, *The Search for Dark Matter*. Scientific American, March 2003.
- [5] James Rich, *Fundamentals of Cosmology*. Springer, 1st Edition, 2001.
- [6] D. -M. Mei, Z. -B. Yin, L. C. Stonehill, A. Hime, arXiv:0712.2470v2 [nucl-ex].
- [7] <http://www-thphys.physics.ox.ac.uk/people/SubirSarkar/meetings/IoPRAS/Smith.pdf>.
- [8] W.H. Lippincott, K.J. Coakley, D. Gastler, A. Hime, E. Kearns, D. N. McKinsey, J. A. Nikkel, and L. C. Stonehill, arXiv:0801.1531v4 [nucl-ex].
- [9] Tarek Saab, *Modern Phys. Lett. A*. 23, 7 (2008).
- [10] MiniCLEAN Conceptual Design Report.
- [11] D. Yu. Akimov, et. al., *Phys. of Atomic Nuclei* 66, 3 (2003).
- [12] The Dark Matter Scientific Assessment Group (DMSAG), Report on the Direct Detection and Study of Dark Matter
- [13] [http://www.sno.phy.queensu.ca/sno/papers/nim\\_paper\\_99.pdf](http://www.sno.phy.queensu.ca/sno/papers/nim_paper_99.pdf)
- [14] Joanne C. Zwinkels, W. F. Davidson, C. X. Dodd, *Applied Optics* 29, 22 (1990).
- [15] Fraser Duncan, SNO Acrylic.
- [16] Jun Cao, arXiv:hep-ex/0509041v1.
- [17] [http://dayabay.physics.hku.hk/underground/talks/DayaBay\\_Reactor\\_Neutrino\\_Experiment.pdf](http://dayabay.physics.hku.hk/underground/talks/DayaBay_Reactor_Neutrino_Experiment.pdf)
- [18] Private communications with Bryce Littlejohn.
- [19] David J. Griffiths, *Introduction to Electrodynamics*, 3rd Edition, 2008.
- [20] [http://www.teknolab.no/pdf/Starna\\_Ref\\_Materials\\_Mol\\_Fluorescence\\_Catalog\\_Complete.pdf](http://www.teknolab.no/pdf/Starna_Ref_Materials_Mol_Fluorescence_Catalog_Complete.pdf).